



Cite this: *Phys. Chem. Chem. Phys.*,
2023, 25, 8651

Mechanical and thermal properties of graphyne-coated carbon nanotubes: a molecular dynamics simulation on one-dimensional all-carbon van der Waals heterostructures†

Jian Li, Penghua Ying, Ting Liang, Yao Du,^a Jianli Zhou^a and Jin Zhang ^{*a}

The mechanical and thermal properties of a hybrid nanotube consisting of a coaxial carbon nanotube (CNT) inside a graphyne nanotube (GNT), *i.e.*, CNT@GNT, are investigated in this paper by using molecular dynamics simulations. The results show that the mechanical properties of CNT@GNT under uniaxial tension depend on the nanotube chirality of its components. Specifically, the Young's modulus of the CNT@GNT structure with an inner zigzag CNT is larger than that of its counterpart with an armchair CNT, while CNT@GNT with an armchair CNT and a zigzag GNT is found to possess the largest tensile strength and fracture strain. In addition, a unique fracture behavior of the successive rupture of its two components is observed in CNT@GNT. The thermal conductivity of CNT@GNT is found to be almost independent of the nanotube chirality of its components but increases as the length and diameter of the CNT@GNT increase. Moreover, strain engineering is shown as an effective avenue to modulate the thermal conductivity of CNT@GNT, which can be enhanced by tension but reduced by compression. The analysis of the phonon spectrum and spectral energy density demonstrates that this strain effect originates from changes of the phonon group velocity and phonon scattering in the strained CNT@GNT.

Received 5th December 2022,
Accepted 19th February 2023

DOI: 10.1039/d2cp05673a

rsc.li/pccp

1. Introduction

As one of the most important members of carbon allotropes, carbon nanotubes (CNTs) have received a lot of attention since their discovery in 1991¹ due to their extraordinary mechanical and thermal properties. An increasing number of studies on the heat conduction of CNTs have been evoked both experimentally and theoretically. According to previous studies, CNTs have ultra-high Young's modulus and thermal conductivity.^{2–10} For example, numerous experimental studies have shown that CNTs have an incredibly high thermal conductivity of more than $3000 \text{ W m}^{-1} \text{ K}^{-1}$ ^{6,7} and an incredibly high Young's modulus of around 1 TPa .^{2,3} Meanwhile, simulation methods such as molecular dynamics (MD) and density functional theory (DFT) are also used to examine many characteristics of CNTs. In previous simulation investigations, superior heat

transport properties are also observed in CNTs, though a significant amount of variation exists in the reported thermal conductivity of CNTs, which may be attributed to the effect of length,¹¹ chirality,¹² strain,¹³ temperature,¹⁴ defects,¹⁵ and the number of walls.¹⁶ The high thermal conductivity and Young's modulus enable CNTs to be treated as suitable reinforcements in a variety of materials including metals and polymers. Specifically, it is proven that the thermal conductivity of these composites can be greatly improved even when only a small amount of CNTs is added.^{17,18}

Graphyne is another nanoallotrope with uniformly distributed sp and sp^2 hybridized carbon atoms and was first proposed by Baughman *et al.* in 1987.¹⁹ Compared to graphene, the presence of C-C triple bonds makes graphyne have many distinct mechanical and thermal properties though they both consist of only carbon atoms.²⁰ In terms of the number of acetylenic linkages, other members of the graphyne family (graph-*n*-yne, *n* = 2, 3, 4, and 5) can be obtained, which have wide applications in fields of catalysis²¹ and water purification.²² Similar to CNTs, graphyne nanotubes (GNTs) can be seen as seamless cylinders rolled up by graphyne sheets. The mechanical and thermal properties of GNTs are similarly different from those of their CNT counterparts due to the existence of C-C triple bonds in GNTs. Specifically, the

^a School of Science, Harbin Institute of Technology, Shenzhen 518055, P. R. China.
E-mail: jinzhang@hit.edu.cn

^b Department of Electronic Engineering and Materials Science and Technology Research Center, The Chinese University of Hong Kong, Shatin, N.T., Hong Kong 999077, P. R. China

† Electronic supplementary information (ESI) available. See DOI: <https://doi.org/10.1039/d2cp05673a>

thermal conductivity^{23,24} and Young's modulus^{25–27} of GNTs are found to be lower than those of CNTs with the same diameter and length. Nevertheless, the light weight, high available surface area and excellent chemical stability of GNTs make them attractive in the application of hydrogen storage^{28,29} and catalyst support.^{30,31} In addition, GNTs are reported to have a great lithium storage capacity due to their unique electronic properties, becoming one of the most promising candidates for sodium-ion battery anode materials.³²

It is known that one-dimensional (1D) tubular nanomaterials that possess different structures and diverse properties can be combined with each other to make up for their own weaknesses. In recent years, 1D heterostructures such as the concentric CNT and boron nitride nanotube (CNT@BNNT)³³ and the concentric CNT and molybdenum disulfide nanotube (CNT@MSNT)³⁴ have attracted a lot of attention. Along with the successful fabrication of these 1D heterostructures, the study of their material properties currently is also receiving attention from the scientific community. For instance, the mechanical and thermal properties of CNT@BNNT³⁵ and CNT@MSNT³⁶ have been widely investigated in many studies. In addition to the aforementioned hybrid nanotubes containing tubular components with different elements, a hybrid nanotube model also can be constructed with different tubular nanoallotropes of only carbon, such as the concentric CNT and GNT, *i.e.*, CNT@GNT. Actually, very recently, Lv *et al.*³⁷ successfully synthesized the CNT@GNT structure with a CNT core coated with the GNT with two acetylenic linkages. The CNT@GNT is also proven to possess excellent conductivity, abundant and uniform reactive sites, low redox potential, more negative surface, and large specific surface, which render it appealing in future catalytic applications.³⁷ However, to our best knowledge, the mechanical and thermal properties of the CNT@GNT structures remain almost unexplored.

In the current study, we use MD simulations to examine the mechanical and thermal properties of CNT@GNT. Specifically, the MD-based tensile tests are used to investigate the Young's modulus, tensile strength and fracture strain of CNT@GNT, while non-equilibrium molecular dynamics (NEMD) simulations

are used to study its thermal conductivity. The dependence of the mechanical and thermal properties of CNT@GNT on the chirality of its component nanotubes is comprehensively discussed. Meanwhile, a thorough discussion of the effects of geometry (length and diameter) and external mechanical stimuli on the thermal conductivity of CNT@GNT are presented. In addition, efforts are also made to reveal the mechanism behind the influence of these factors on the mechanical and thermal properties of CNT@GNT.

2. Computational methods

2.1. Models

The structure of the coaxial CNT inside the GNT, *i.e.*, CNT@GNT is shown in Fig. 1(a). The distance between the inner CNT layer and the outer GNT layer is set as 3.4 Å, equal to the interlayer distance of multi-walled CNTs³⁸ and close to the value of multi-walled GNTs.³⁹ As shown in Fig. 1(b), the graphene (or the rolled CNT) and graphyne (or the rolled GNT) have two principle directions, *i.e.*, armchair and zigzag directions. Thus, CNT@GNT could have four different lattice structures after reassembling zigzag or armchair nanotubes (CNT and GNT) together. The four structures of CNT@GNT are noted as AA, AZ, ZA and ZZ. Here, "A" and "Z" stand for the armchair and zigzag, respectively. Moreover, the first and second letters represent the nanotube chirality of the inner CNT and the outer GNT, respectively. For instance, the AZ nanotube represents the CNT@GNT composed of an inner armchair CNT and an outer zigzag GNT.

Due to the different lattice constants between CNTs and GNTs, there will exist the length mismatch or the residual stress in the CNT and GNT components of CNT@GNT. In order to reduce the residual stress, a paring with the smallest value of the percentage of length mismatch is needed. Specifically, armchair CNTs with 82 and 78 unit cells in the axial direction are paired to armchair GNTs with 29 unit cells and zigzag GNTs with 16 unit cells, respectively, while zigzag CNTs with 46 and 45 unit cells are paired to armchair GNTs with 28 unit cells and

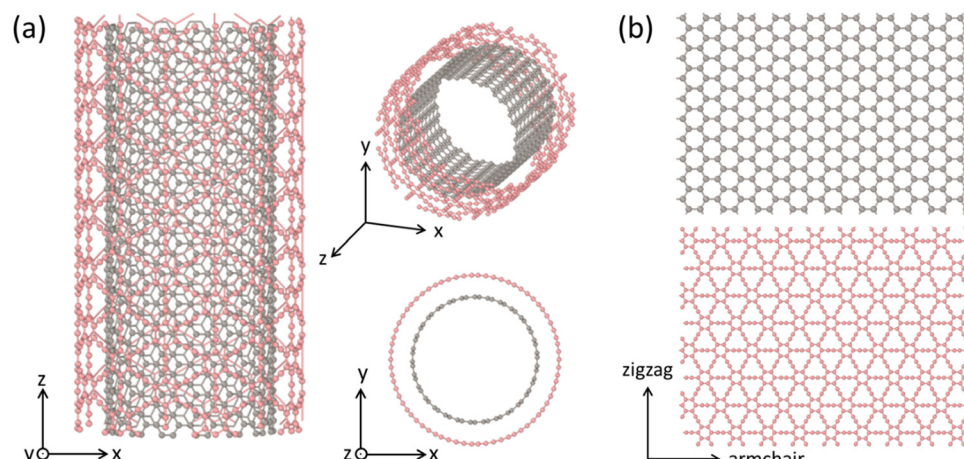


Fig. 1 (a) The structure of CNT@GNT. (b) The nanotube chirality of the components CNT and GNT.

zigzag GNTs with 16 unit cells, respectively. More details about the AA, AZ, ZA and ZZ structures of CNT@GNT considered here are provided in the ESI.[†]

2.2. MD simulations on the mechanical properties

MD simulations conducted here were performed using the large-scale atomic/molecular massively parallel simulator (LAMMPS) package.⁴⁰ The velocity Verlet algorithm with a time step of 0.5 fs was employed to integrate the equations of motion. The periodic boundary conditions were applied in the axial direction. In MD simulations, the adaptive intermolecular reactive empirical bond order (AIREBO) potential⁴¹ derived from the second-generation Brenner potential was used to describe the short-range C–C interactions in component CNT and GNT layers as well as the long-range van der Waals (vdW) interaction between CNT and GNT layers. The AIREBO potential has been employed in many previous MD simulations to successfully reveal the mechanical properties of various carbon nanoallotropes, such as individual CNT,⁴² GNT,²⁵ graphene,⁴³ and graphyne.²⁶ According to a previous study,⁴⁴ the mechanical properties, especially fracture behaviors of carbon nanomaterials, are very sensitive to the inner cutoff radius in AIREBO potential, since the selection of an appropriate cutoff function parameter can avoid the unrealistic hardening behavior observed at high strains near the fracture and thus is crucial to obtain reliable results. Here, we chose the recommended cutoff of 2.0 Å,⁴⁴ which has the capacity to more realistically describe the maximum elongation and fracture mechanism of carbon nanomaterials.

Before conducting the mechanical study of CNT@GNT, the conjugate gradient method was used to conduct the energy minimization of all initial structures. In order to obtain the equilibrium states of all considered CNT@GNT, isothermal-isobaric (or *NPT*) and canonical (or *NVT*) ensembles were successively used to equilibrate the structures for 100 ps, in which the Nosé–Hoover⁴⁵ thermostat and barostat were employed with a temperature of 300 K and zero pressure. After

obtaining its equilibrium structures, the CNT@GNT was subjected to an external strain by gradually elongating the length of the simulation box with a strain rate of 10^9 s⁻¹ along the axial direction. Specifically, as shown in Fig. 2(a), in this stretching process, constraints were applied at both ends of CNT@GNT to prevent the serious drifting effects during the energy minimization. During the elongation process, the strain was defined as $\varepsilon = (l - l_0)/l_0$ with l_0 and l , respectively, being lengths of the initial and deformed structures, while the stress was calculated as the arithmetic mean of local stresses on all atoms.

2.3. NEMD simulations on the heat transport properties

The thermal conductivity of CNT@GNT at room temperature (300 K) was evaluated by using NEMD simulations, which were similarly implemented using the LAMMPS package together with the AIREBO potential.⁴¹ Although due to its underestimation of the phonon group velocity, the AIREBO potential is reported to underestimate the thermal conductivities of some carbon nanomaterials, such as CNTs and graphene, the AIREBO potential explicitly takes into account the σ and π interactions between carbon atoms, which thus can improve the description of carbon nanomaterials with mixed single, double and triple C–C bonds.²³ Thus, the AIREBO potential has widely been employed in describing many complex carbon nanomaterials to provide a more accurate description of their lattice dynamics and phonon thermal transport behaviors.^{46,47}

All CNT@GNT structures considered in NEMD simulations were obtained after conducting a similar energy minimization process mentioned above except that the Langevin⁴⁸ thermostat rather than the Nosé–Hoover thermostat was employed here. To implement NEMD simulations, as shown in Fig. 2(b), a CNT@GNT structure was divided into five sections. Specifically, two fixed sections locate at two ends of the nanotube. One hot source section and one cold source section are adjacent to the fixed sections. One middle free section is sandwiched between the hot and cold sources, which was further divided into 16

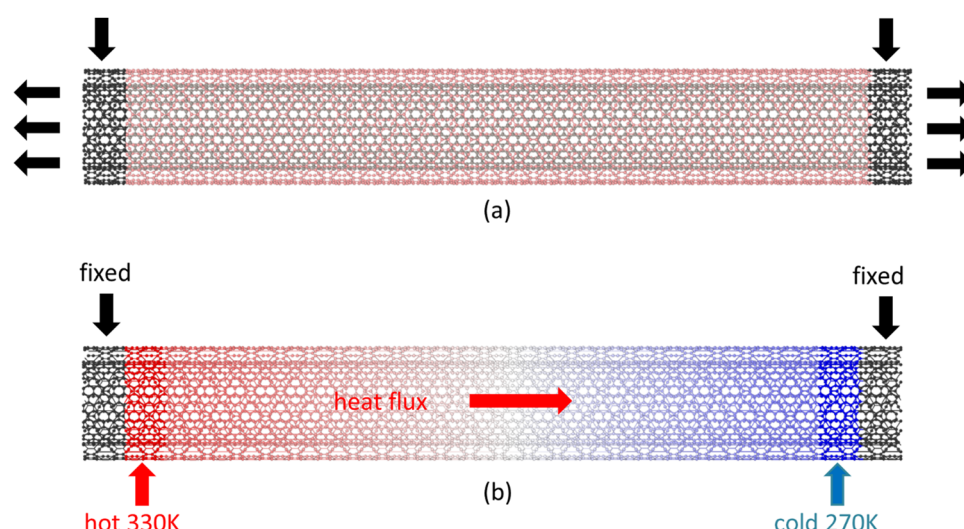


Fig. 2 (a) MD simulation set-up for the uniaxial tensile test. (b) NEMD simulation set-up for the calculation of thermal conductivity.

slabs along the axial direction to better analyze the temperature distribution. Here, temperatures of hot and cold sources were, respectively, set to be 10% above and below the room temperature, *i.e.*, 330 K and 270 K. In this process, the heat will flow from the hot source section to the cold source section. In order to form a stable heat flow in the middle free section, the heat transport simulations with at least 2 ns were performed in the microcanonical (or *NVE*) ensemble. A stable temperature distribution was achieved after the simulations with 2 ns. Thus, the temperature distribution in the free section was obtained by averaging over another extra 1 ns MD simulation.

After obtaining the stable temperature distribution, the following Fourier's law of heat conduction⁴⁹ can be utilized to calculate the thermal conductivity of CNT@GNT.

$$k = \frac{J}{\text{grad}T \cdot A}, \quad (1)$$

Here J denotes the heat flux along the axial direction of CNT@GNT. $\text{grad}T$ is the temperature gradient along the axial direction, which can be calculated from the slope of the obtained temperature-position diagram. A is the cross-sectional area of CNT@GNT, which can be calculated as $A = \pi d_1 h_1 + \pi d_2 h_2$ with d_1 and d_2 being the diameters and h_1 and h_2 being the thicknesses of the CNT and GNT, respectively. In this study, the thicknesses of the CNT and GNT components, *i.e.*, h_1 and h_2 , were similarly set to 3.4 Å.⁵⁰

3. Results and discussion

3.1. Mechanical properties

Based on the MD simulation technique introduced above, we obtained the stress-strain relationships of the considered four structures of CNT@GNT, whose components have different nanotube chiralities. All considered CNT@GNT structures have the same length of 200 Å and the same diameter of 27.5 Å. Here, the diameter of CNT@GNT was set similar to the diameter of its outer GNT component. The obtained results are graphically shown in Fig. 3. It is found that at relatively low strains, the

stress increases linearly with increasing strain. The slope of the linear part of the stress-strain curve is equal to the Young's modulus. The obtained Young's moduli of four CNT@GNT structures are shown in Fig. 4. The Young's moduli of AA and AZ structures are found to be almost similar to each other, which are around 615 GPa. The almost same Young's moduli are similarly observed in ZA and ZZ structures, though their values are about 9.7% higher than the results of their AA and AZ counterparts. This result indicates that in terms of their structures, the Young's modulus of CNT@GNT structures is majorly determined by the chirality of their CNT components, which is attributed to the fact that the difference between Young's moduli of zigzag and armchair CNTs is larger than that of their GNT counterparts. Indeed, based on similar MD simulations on individual CNTs and GNTs, we find that the Young's modulus of 942 GPa of zigzag CNT is 12.1% higher than 840 GPa of its armchair counterpart, while the Young's modulus of 431 GPa of zigzag GNT is only 5.9% smaller than 458 GPa of armchair GNT. Thus, the Young's modulus of ZA and ZZ structures is expected to be larger than that of their AA and AZ counterparts, which is consistent with our MD results.

Moreover, the Young's moduli of all CNT@GNT structures are found to range between the values of CNTs and GNTs. From viewpoints of continuum mechanics, a CNT@GNT structure can be equivalently modelled as a composite shell model consisting of inner (CNT) and outer (GNT) component shells with Young's moduli being Y_1 and Y_2 and diameters being d_1 and d_2 , respectively. Thus, according to the composite theory, when an axial strain ϵ is applied, the stress generated in CNT@GNT is $\sigma \approx \epsilon(Y_1 d_1 + Y_2 d_2)/(d_1 + d_2)$. In other words, the equivalent Young's modulus of CNT@GNT predicted from the composite shell models is $Y \approx (Y_1 d_1 + Y_2 d_2)/(d_1 + d_2)$. Based on the values of Y_1 and Y_2 extracted from above MD simulations, the Young's moduli of AA, AZ, ZA and ZZ structures predicted from the composite model are 621, 606, 664 and 650 GPa. These theoretically predicted results are close to the results obtained from MD simulations.

We also observe a complex fracture behavior in all CNT@GNT structures, which generally contains two significant stress drop processes in their stress-strain curves as shown in Fig. 3. Specifically, the first stress drop signifies the onset of fracture of CNT@GNT structures. The corresponding stress and strain at the first stress drop are termed the tensile strength and the fracture strain, respectively. As shown in Fig. 4, among four CNT@GNT structures considered here, the AZ structure possesses the largest tensile strength and fracture strain of 72 GPa and 0.171, which are followed by 64 GPa and 0.131 of the ZZ structure. The smallest tensile strength and fracture strain are found in AA and ZA structures. Moreover, the tensile strength and fracture strain of AA and ZA structures are also found to be close to each other, which are around 55 GPa and 0.110. After the first stress drop, the stress can still increase with the increasing strain, indicating the breaking of only some components of CNT@GNT and still the maintenance of its structural integrity. However, the stress in all CNT@GNT structures can suddenly drop to zero after the second stress drop, indicating the complete

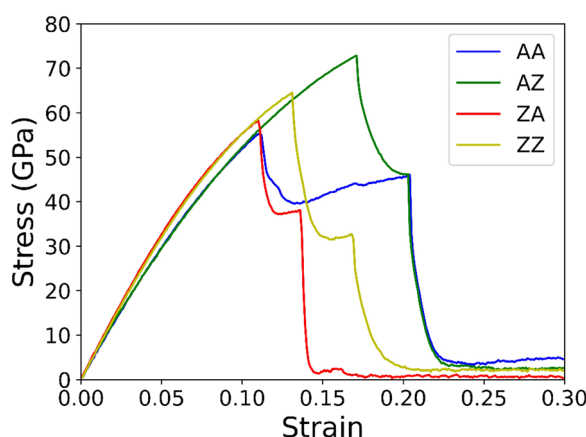


Fig. 3 Stress-strain curves of four CNT@GNT structures under tension, whose component nanotubes have different chiralities.

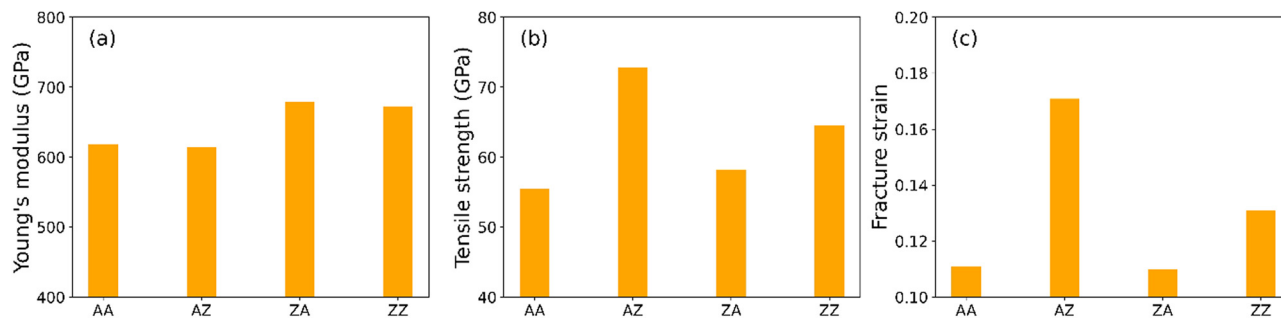


Fig. 4 A comparison of (a) Young's modulus, (b) tensile strength, and (c) fracture strain among different CNT@GNT structures.

fracture of the entire CNT@GNT structures. In addition, the duration of the process between the onset of fracture and the final fracture is significantly sensitive to the structure of CNT@GNT. Specifically, this process is most obvious in the AA structures but less obvious in their AZ counterparts. In order to better explain the complex fracture behaviors of CNT@GNT structures, we show in Fig. 5 the evolution of stress in their CNT and GNT components during the stretching process. We find that the fracture strain of CNT@GNT is identical to the smallest value of the fracture strains of their CNT and GNT components, while the strain at the final fracture corresponds to the largest fracture strain of their components. Thus, the duration of the process between the onset of fracture and the final fracture is determined by the difference between the fracture strains of their CNT and GNT components.

Theoretically, it is known that the deformation compatibility requires two coaxial components of CNT@GNT to have the same axial strain during the stretching process. Thus, the fracture will initiate in the component with a lower fracture strain. Because the fracture strain of armchair CNT is larger than that of zigzag and armchair GNT, the fracture of AA and AZ structures is thus expected to start in their outer GNT component. The fracture of the ZA structures is similarly expected to start in their outer GNT component, since the fracture strain of zigzag CNT is also larger than that of the armchair GNT. However, the fracture strain of zigzag GNT turns to be larger than that of the zigzag CNT. Thus, the fracture of the ZZ structures is expected to uniquely start in their inner CNT component. To prove this prediction, we show in Fig. 6 the structures and von Mises stress distributions of four CNT@GNT

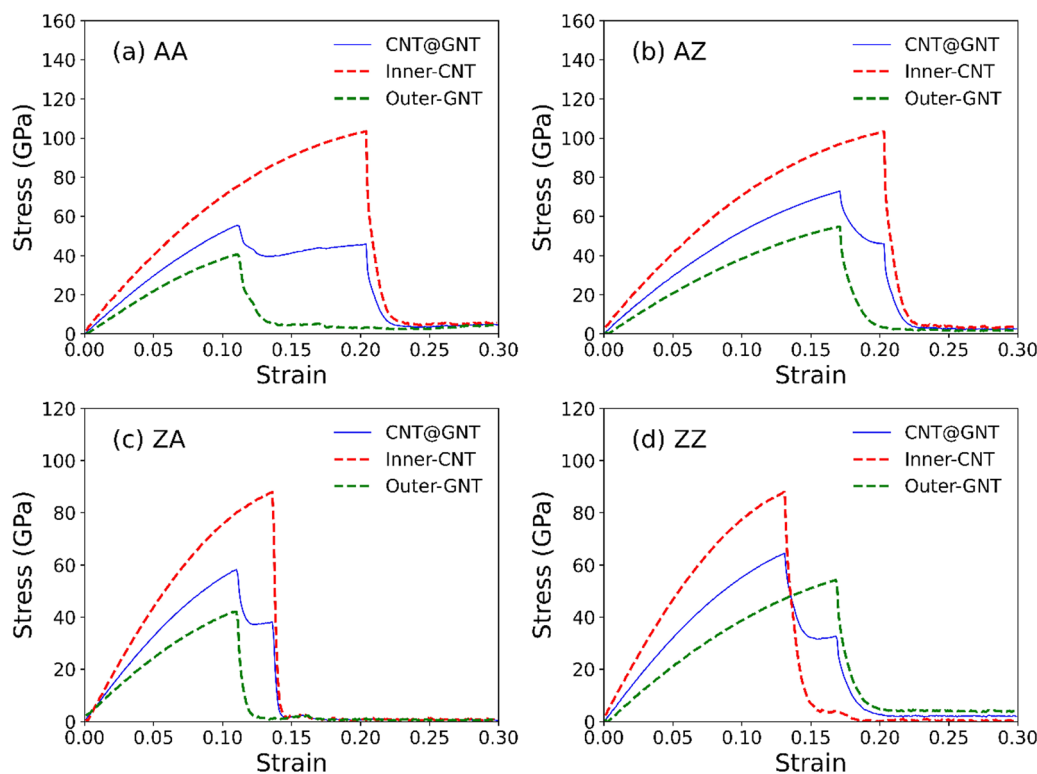


Fig. 5 The stress in the entire structure and component nanotubes of (a) AA, (b) AZ, (c) ZA, and (d) ZZ structures during the tension process of CNT@GNT.

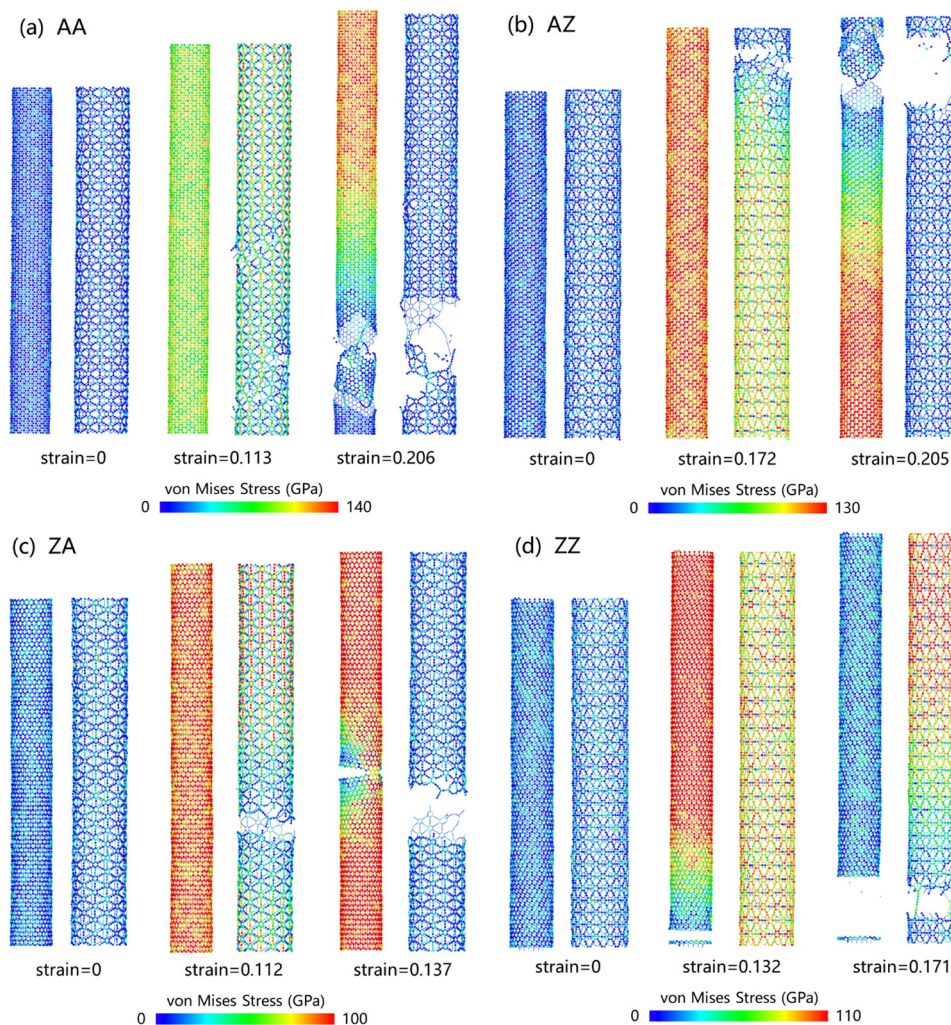


Fig. 6 The deformation processes and von Mises stress evolution of component nanotubes of (a) AA, (b) AZ, (c) ZA, and (d) ZZ structures during the tension process of CNT@GNT.

structures just at the strains of the onset of fracture and the final fracture. Indeed, except the ZZ structures whose fracture starts in their CNT components, the fracture of all other three CNT@GNT structures is found to start in their GNT components. Moreover, the fractured CNT and GNT components both almost cannot retain their structural integrity. Thus, the deformation of the entire CNT@GNT structure in the process between the onset of fracture and final fracture is totally resisted by the remaining nanotube components, such as the CNT in AA, AZ and ZA structures but the GNT in ZZ structures.

The effect of geometric size on the mechanical properties of CNT@GNT is finally examined. As a typical example, only the AA structure was considered here. In addition, AA structures with the same diameter of 27.5 Å but different lengths ranging from 100 Å to 600 Å were considered to study the effect of length (see Fig. 7a), while their counterparts having the same length of 200 Å but different diameters ranging from 19.6 Å to 39.3 Å were considered to study the effect of diameter (see Fig. 7b). As shown in Fig. 7, both the length and diameter have trivial effects on the Young's modulus, tensile strength and

fracture strain of CNT@GNT, in spite of small variations observed in these mechanical parameters of CNT@GNT with different lengths and diameters. Actually, in previous MD studies on GNTs and multi-walled CNTs,^{27,51} the geometric size is similarly found to have a trivial effect on their mechanical properties.

3.2. Thermal properties

By using NEMD simulations detailed in Section 2.2, we investigated the thermal conductivity of CNT@GNT in this subsection. As a typical example, in Fig. 8(a), we show the temperature distribution in the AA structure. A linear temperature change is observed between the hot slab and cold slab, which indicates a constant heat flux in CNT@GNT. Meanwhile, as shown in Fig. 8(b), magnitudes of the energy flux passing the hot slab and cold slab are identical to each other, indicating the conservation of total energy. Based on the obtained heat flux and the temperature gradient, the thermal conductivity can be calculated from eqn (1).

In Fig. 9, we compare the thermal conductivities of AA, AZ, ZA and ZZ structures of CNT@GNT. Here, all CNT@GNT

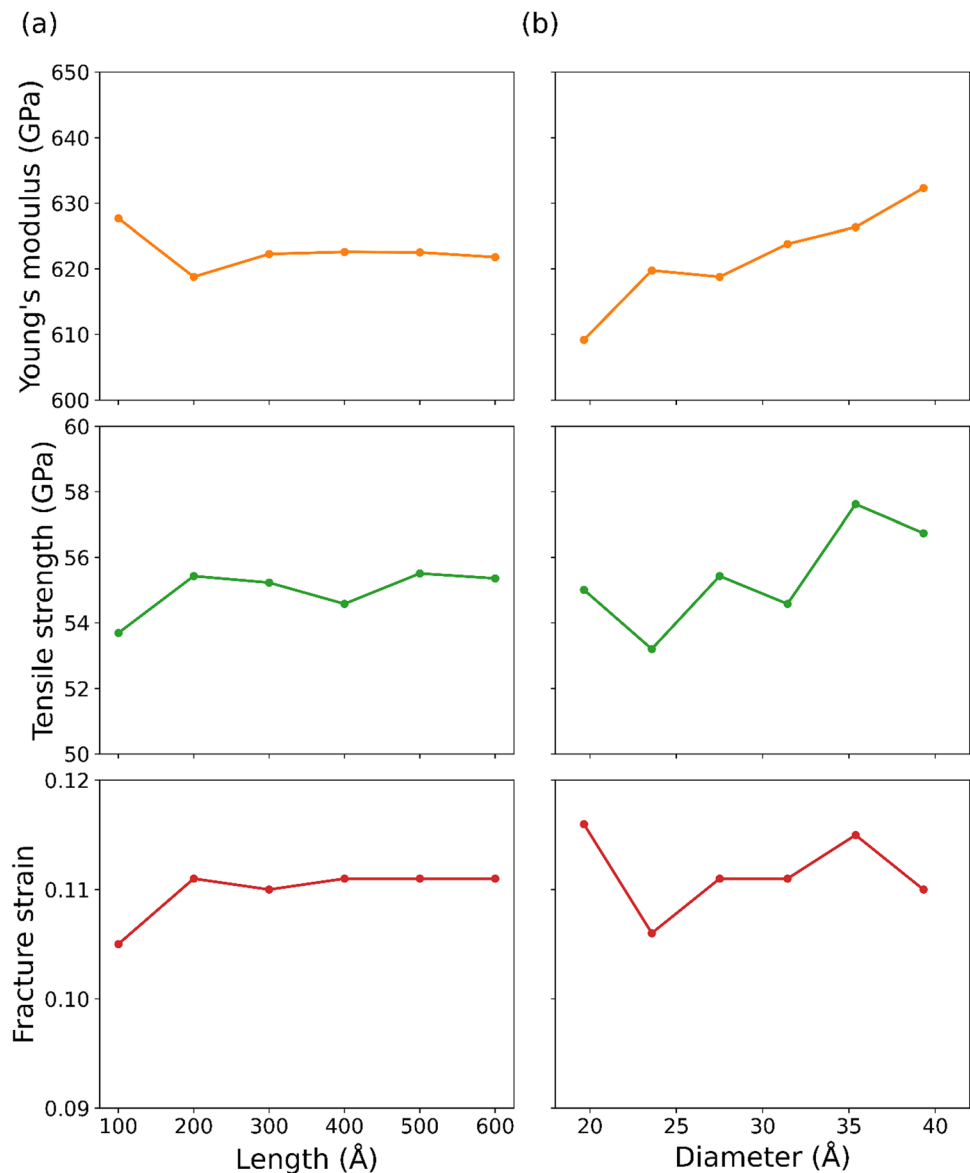


Fig. 7 Young's modulus, tensile strength, and fracture strain of CNT@GNT with different (a) lengths and (b) diameters.

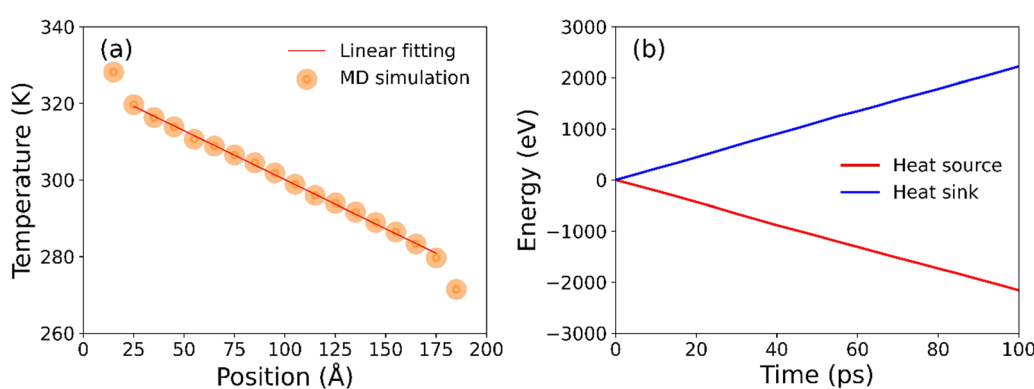


Fig. 8 (a) Temperature distribution in CNT@GNT obtained from NEMD simulations at 300 K. (b) Energies added to the heat source and removed from the heat sink during the simulation.

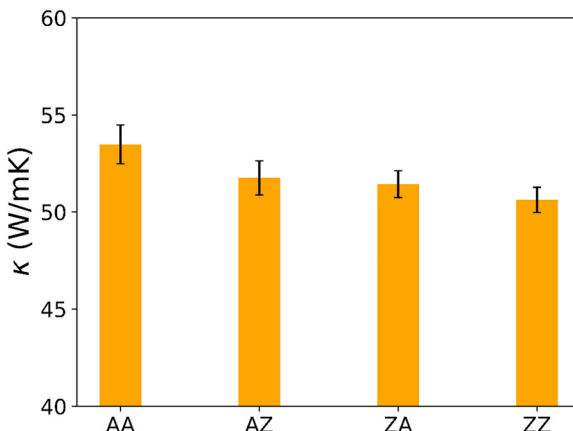


Fig. 9 A comparison of thermal conductivity among different CNT@GNT structures.

structures have the same length around 200 Å and the same diameter around 27.5 Å. In addition, three individual calculations were conducted for each CNT@GNT structure, the average of which was taken as the final result. Our results show that the thermal conductivity of CNT@GNT is almost independent of its structure. Specifically, the thermal conductivities of CNT@GNTs with different structures increase and decrease around the mean value of $51 \text{ W m}^{-1} \text{ K}^{-1}$. The deviation of this average value from the maximum or minimum thermal conductivity is less than 4%. The thermal conductivity of CNT@GNT is between the values of CNTs and GNTs, since, as mentioned before, CNT@GNT can be equivalently regarded as a composite structure consisting of CNT and GNT components. The structure-independence of thermal conductivity can be understood by the fact that the thermal conductivities of CNTs and GNTs are almost independent of nanotube chirality (see the ESI†). Some existing studies have concluded that, in contrast to the electronic conductivity, the thermal conductivity is insensitive to nanotube chirality.¹² According to these studies, the electron density of states depends on the chirality while the chirality dependence is absent from the phonon density of states. When the chirality and diameter considered are interchangeable, the effect of nanotube chirality on the thermal conductivity is trivial unless the thermal

transport is dominated by the electron transport. Considering the fact that the thermal conductivity of CNT@GNT is almost independent of its structure, only the AA structure was considered in the following discussion to simplify our analysis without losing generality.

In Fig. 10(a), we show the thermal conductivities of CNT@GNT structures with different lengths ranging from 100 Å to 600 Å. Here, all considered CNT@GNT structures have the same diameter of 27.5 Å. The thermal conductivity is found to increase from $36 \text{ W m}^{-1} \text{ K}^{-1}$ to $76 \text{ W m}^{-1} \text{ K}^{-1}$ as the length of the nanotube increases from 100 Å to 600 Å, though the increase rate gradually reduces in this process. A similar phenomenon that the thermal conductivity increases with the increasing length also has been observed in single-walled⁵² and multi-walled CNTs.⁵³ Theoretically, the scattering-dominated thermal transport phenomena can be the cause of the increase in thermal conductivity with the increasing length. The length dependence of thermal conductivity disappears when the length exceeds the phonon mean free path (MFP) because the transport process switches from ballistic regime to diffusive regime. The relationship between the thermal conductivity of CNT@GNT k and its length L can be expressed as follows using the kinetic theory⁵⁴:

$$\frac{1}{k} = \frac{1}{k_\infty} \left(\frac{l_p}{L} + 1 \right), \quad (2)$$

where k_∞ is the thermal conductivity of CNT@GNT with an infinite length and l_p is the effective phonon MFP. In Fig. 10(b), we show the relationship between the inverse thermal conductivity ($1/k$) and the inverse length of CNT@GNT ($1/L$), as well as their linear fitting. We can see that eqn (2) can fit the MD results shown in Fig. 9(b) very well.

The diameter may be another geometric parameter affecting the thermal conductivity of CNT@GNT in addition to the length. As shown in Fig. 11, although the increase of diameter can induce an increase in thermal conductivity of CNT@GNT, the change of thermal conductivity in this process is small. For example, the thermal conductivity increases by 28.6% when the diameter increases from 19.6 Å to 39.3 Å. The change of thermal conductivity with increasing diameter is consistent with the results previously observed in CNTs^{10,11} and CNT@BNNT.³⁵

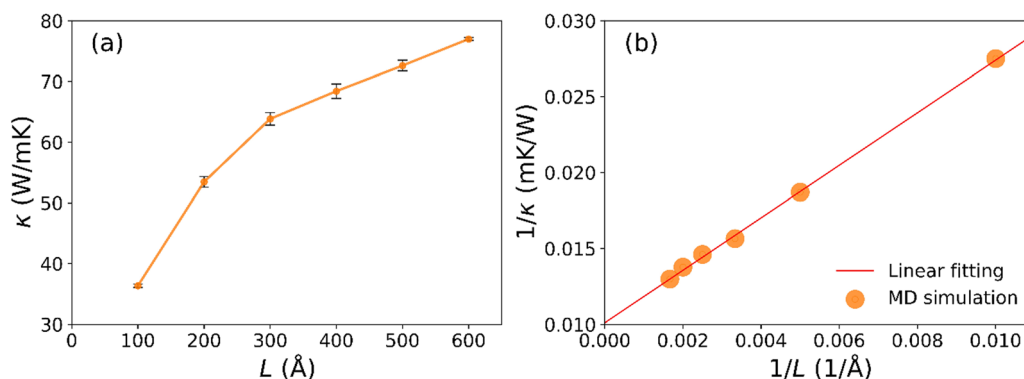


Fig. 10 (a) Thermal conductivity of CNT@GNT with different lengths. (b) Relationship between the inverse thermal conductivity and the inverse length of CNT@GNT.

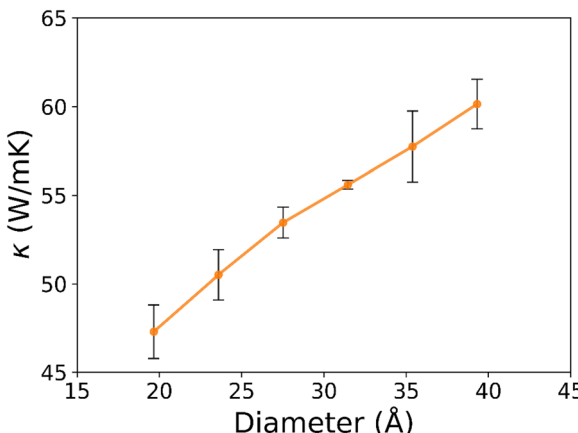


Fig. 11 Thermal conductivity of CNT@GNT with different diameters.

The thermal conductivity is expected to eventually stabilize at a constant value with a further increase in the diameter of CNT@GNT. However, our calculations do not show a noticeable convergence, which is probably due to the narrow range of diameters taken into account in the investigation.

In addition to the geometry, we also examined the effect of some external stimuli such as the mechanical loading on the thermal conductivity of CNT@GNT, since strain engineering is proven to be an efficient method to modulate the heat transport properties of many carbon nanomaterials.^{55,56} To investigate the effect of external mechanical loading or the axial strain on the thermal conductivity, we first stretched CNT@GNT to a specified strain and then calculated the thermal conductivity of the strained structure at its equilibrium state. In Fig. 12, we show the thermal conductivity of CNT@GNT across a wide range of compressive and tensile axial strains ranging from -4% to 10%. Specifically, the stress-strain curve of the CNT@GNT under compression is shown in Fig. S1 (see the ESI†). It is found that buckling instability occurs at a compressive strain of -3.2%. Thus, structures at compressive strains of -2% and -4% were considered here to be treated as the representative structures before and after the buckling instability, respectively. As can be

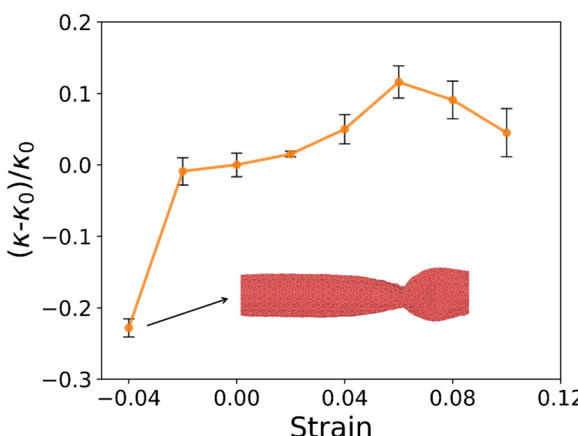


Fig. 12 Thermal conductivity of CNT@GNT at different axial strain states. The inset shows the buckling of CNT@GNT at a compressive strain of 4%.

seen in Fig. 12, the compression can generally reduce the thermal conductivity of strained CNT@GNT. For example, the thermal conductivity of CNT@GNT can be reduced by 22.8% when the magnitude of the compressive strain increases to 4%. However, when tension is applied, a nonmonotonic change of the thermal conductivity is observed as the tensile strain increases. For example, when the tensile strain reaches 6%, the thermal conductivity of CNT@GNT reaches its maximum value and increases by 11.6% compared to its initial value. However, as the strain continues to increase, the thermal conductivity begins to decrease. A similar nonmonotonic change of the thermal conductivity with varying tensile strains also has been observed in previous studies of CNTs.^{11,13}

The frequency of phonons and density of particular frequency are important to understand the amount of thermal energy transferred due to the strain effect. Therefore, the phonon density of states (PDOS), which measures the quantity of vibrational modes per unit frequency, can be an important tool to explain the strain effect on the thermal transport characteristics of CNT@GNT observed above. Here, the normalized PDOS was calculated by applying the Fourier transformation to velocity autocorrelation functions of the simulated CNT@GNT systems⁵⁷:

$$\text{PDOS}(\omega) = \frac{\sum_{i=1}^N v_i(0) \cdot v_i(t)}{\sum_{i=1}^N v_i(0) \cdot v_i(0)} \cdot \exp(-2\pi i \omega t) dt, \quad (3)$$

where N is the total number of atoms in the CNT@GNT system, ω is the phonon frequency, i is the imaginary unit, and $v_i(t)$ and $v_i(0)$ are velocities of the i th carbon atom at the moment t and initial time, respectively.

The normalized PDOS at different axial strains is shown in Fig. 13. In general, we can observe the change in the PDOS of CNT@GNT due to the external loading, which indicates different phonon properties in the strained CNT@GNT. According to the classical lattice thermal transport theory, the thermal conductivity can be expressed as $k = \sum_m c v_m l$, where m , c , v_m

and l represent the phonon modes, specific heat, group velocity and MFP, respectively.⁵⁸ Since the PDOS of CNT@GNT under mechanical loading is different from that of its counterpart without strain, it is thus believed that the strain may affect the thermal transport properties of CNT@GNT via modifying its phonon properties. In addition, when the amplitude of compressive strain is up to 4%, buckling instability occurs in CNT@GNT as shown in the inset of Fig. 13, which may further trigger the so-called phonon-defect scattering in CNT@GNT.^{59,60} The extra phonon-defect scattering in buckled CNT@GNT will further significantly decrease its thermal conductivity. This theoretical prediction is found to agree well with the NEMD results shown in Fig. 12, in which a dramatic drop in thermal conductivity is observed in the CNT@GNT compressed under a strain of 4%.

To further prove the above mechanism of strain effect on thermal conductivity, we also computed the modal phonon information of CNT@GNT with different strains using the spectral energy density (SED), which represents the average

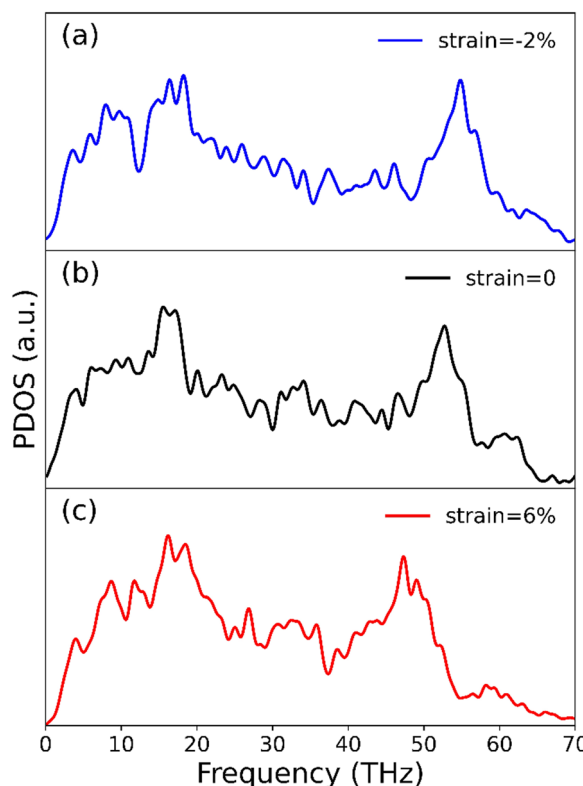


Fig. 13 The calculated PDOS of CNT@GNT at axial strains of (a) -2% , (b) 0 , and (c) 6% .

kinetic energy per unit cell. Specifically, the SED Φ is a function of the wave-vector \vec{k} and the frequency ω , that is⁶¹

$$\Phi(\vec{k}, \omega) = \frac{1}{4\pi\tau_0 N} \sum_{\alpha, b} m_b \left\| \int_0^{\tau_0} \sum_N v_\alpha(N, b) \times \exp[i\vec{k} \cdot \vec{r}(N, 0) - i\omega t] dt \right\|^2, \quad (4)$$

where τ_0 is the integration time, m_b is the mass of atom b , v_α is the atomic velocity along the α direction inside the N th cell, \vec{r} is the equilibrium position vector, and i is the imaginary unit.

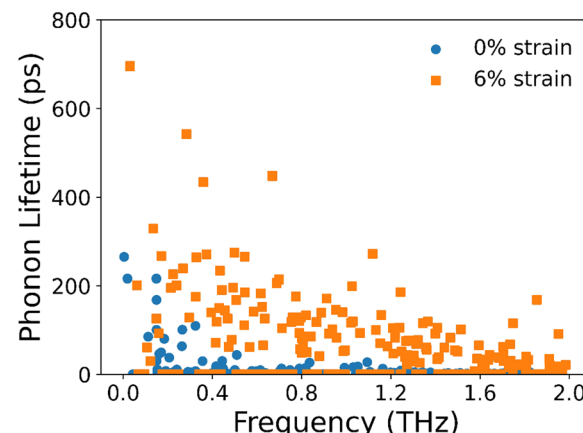


Fig. 15 The phonon lifetime of CNT@GNT under strains of 0 and 6% extracted from SED results.

In this work, we used 40 unit cells in the axial direction to calculate the SED of CNT@GNT. All systems were first relaxed under the *NVT* ensemble for 1 ns and then equilibrated for another 1.5 ns under the *NVE* ensemble. The collected data for last 1 ns were used to obtain the SED along the axial direction when the CNT@GNT is under uniaxial strains of -2% , 0% , and 6% . Furthermore, the region containing the specified peak was selected to fit the peak frequency with the aid of the following Lorentzian function⁶¹:

$$\Phi(\vec{k}, \omega) = \frac{I}{1 + [(\omega - \omega_c)/g]^2}, \quad (5)$$

where I is the peak magnitude, ω_c denotes the frequency at the peak center, and g is the half-width at half-maximum. Thus, based on the treatment in eqn (5), the phonon lifetime can be calculated through $\tau = 1/2g$.

Only the information of the acoustic branches with clear peaks was calculated because of validation purposes. From the SED results shown in Fig. 14, we find that when under a compressive strain of 2% , the SED peaks of CNT@GNT are unclear

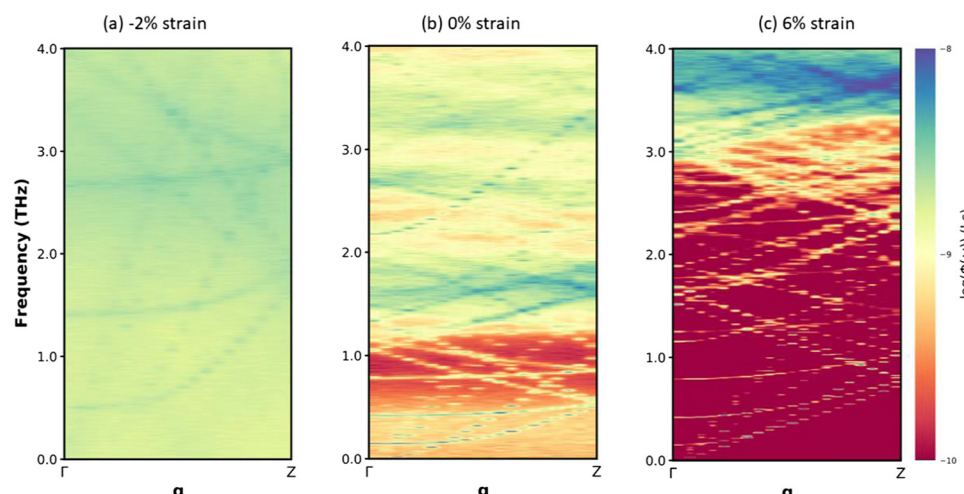


Fig. 14 The SED results of CNT@GNT under axial strains of (a) -2% , (b) 0 , and (c) 6% .

for all phonon modes, indicating a much stronger scattering and correspondingly a shorter phonon lifetime compared with those of CNT@GNT in the absence of loading. In contrast, when under a tensile strain of 6%, the phonon dispersion structure of CNT@GNT becomes much clearer with a thinner linewidth, which indicates a much longer phonon lifetime as shown in Fig. 15. In addition to the change of phonon lifetime, a tensile strain also leads to steeper acoustic branches, which is related to the increment of group velocity.

4. Conclusions

In this paper, the mechanical and thermal properties of CNT@GNT are investigated through a series of MD simulations. The Young's modulus of CNT@GNT is found to range between the values of individual CNTs and GNTs, which is also dependent on the nanotube chirality of its components. The Young's modulus of the CNT@GNT structure with an inner zigzag CNT is specifically larger than that of its counterpart with an armchair CNT. The fracture properties of CNT@GNT are found to exhibit a similar dependence on the chirality of its component nanotubes, since the tensile strength and fracture strain of CNT@GNT are identical to the smallest value between CNTs and GNTs. Moreover, due to the distinct fracture properties between CNTs and GNTs, a unique fracture behavior exhibiting a successive rupture of its two components is observed in CNT@GNT. Different from the mechanical properties of CNT@GNT, the thermal properties are almost independent of the nanotube chirality of its components. Nevertheless, the thermal conductivity of CNT@GNT is found to be strongly dependent on its geometry, which can increase as the length and diameter of CNT@GNT increase. Moreover, our study also indicates that the external stimuli such as mechanical loading can effectively modify the heat transport properties of CNT@GNT. Specifically, the tension and compression can increase and decrease the thermal conductivity of CNT@GNT, which is attributed to the changes of the phonon group velocity and phonon scattering of CNT@GNT during this loading process. Overall, our study provides a comprehensive understanding of the mechanical and thermal properties of CNT@GNT, which is helpful for the engineering applications of this newly synthesized hybrid nanotube in the future.

Conflicts of interest

There are no conflicts to declare.

Acknowledgements

This work was supported by the National Natural Science Foundation of China (Grant No. 11602074), the Natural Scientific Research Innovation Foundation in Harbin Institute of Technology (Grant No. HIT.NSRIF.2020058) and the Guangdong Basic and Applied Basic Research Foundation (Grant No. 2022A1515010631).

References

- S. Iijima, Helical microtubules of graphitic carbon, *Nature*, 1991, **354**, 56–58.
- M. M. J. Treacy, T. W. Ebbesen and J. M. Gibson, Exceptionally high Young's modulus observed for individual carbon nanotubes, *Nature*, 1996, **381**, 678–680.
- G. Van Lier, C. Van Alsenoy, V. Van Doren and P. Geerlings, Ab initio study of the elastic properties of single-walled carbon nanotubes and graphene, *Chem. Phys. Lett.*, 2000, **326**, 181–185.
- J. Liu, Q. Zheng and Q. Jiang, Effect of a rippling mode on resonances of carbon nanotubes, *Phys. Rev. Lett.*, 2001, **86**, 4843–4846.
- X. Wei, Q. Chen, L. Peng, R. Cui and Y. Li, Tensile loading of double-walled and triple-walled carbon nanotubes and their mechanical properties, *J. Phys. Chem. C*, 2009, **113**, 17002–17005.
- P. Kim, L. Shi, A. Majumdar and P. L. McEuen, Thermal transport measurements of individual multiwalled nanotubes, *Phys. Rev. Lett.*, 2001, **87**, 215502.
- E. Pop, D. Mann, Q. Wang, K. Goodson and H. Dai, Thermal conductance of an individual single-wall carbon nanotube above room temperature, *Nano Lett.*, 2006, **6**, 96–100.
- C. W. Padgett and D. W. Brenner, Influence of chemisorption on the thermal conductivity of single-wall carbon nanotubes, *Nano Lett.*, 2004, **4**, 1051–1053.
- K. Sun, M. A. Stroscio and M. Dutta, Thermal conductivity of carbon nanotubes, *J. Appl. Phys.*, 2009, **105**, 074316.
- Z. Ma, Z. Guo, H. Zhang and T. Chang, Extremely high thermal conductivity anisotropy of double-walled carbon nanotubes, *AIP Adv.*, 2017, **7**, 065104.
- S. Nakarmi and V. U. Unnikrishnan, Understanding size and strain induced variabilities in thermal conductivity of carbon nanotubes: A molecular dynamics study, *Mech. Adv. Mater. Struct.*, 2020, **29**, 1977–1985.
- G. Zhang and B. Li, Thermal conductivity of nanotubes revisited: Effects of chirality, isotope impurity, tube length, and temperature, *J. Chem. Phys.*, 2005, **123**, 114714.
- C. Ren, W. Zhang, Z. Xu, Z. Zhu and P. Huai, Thermal conductivity of single-walled carbon nanotubes under axial stress, *J. Phys. Chem. C*, 2010, **114**, 5786–5791.
- A. O. Mohamed and S. Deepak, Temperature dependence of the thermal conductivity of single-wall carbon nanotubes, *Nanotechnology*, 2001, **12**, 21–24.
- J. Park, M. F. P. Bifano and V. Prakash, Sensitivity of thermal conductivity of carbon nanotubes to defect concentrations and heat-treatment, *J. Appl. Phys.*, 2013, **113**, 034312.
- X. Zhang, W. Zhou, X. Chen, Y. Liu and K. Chen, Significant decrease in thermal conductivity of multi-walled carbon nanotube induced by inter-wall van der Waals interactions, *Phys. Lett. A*, 2016, **380**, 1861–1864.
- M. J. Biercuk, M. C. Llaguno, M. Radosavljevic, J. K. Hyun, A. T. Johnson and J. E. Fischer, Carbon nanotube composites for thermal management, *Appl. Phys. Lett.*, 2002, **80**, 2767–2769.
- A. M. K. Esawi, K. Morsi, A. Sayed, M. Taher and S. Lanka, Effect of carbon nanotube (CNT) content on the mechanical

- properties of CNT-reinforced aluminium composites, *Compos. Sci. Technol.*, 2010, **70**, 2237–2241.
- 19 R. H. Baughman, H. Eckhardt and M. Kertesz, Structure-property predictions for new planar forms of carbon: Layered phases containing sp₂ and sp atoms, *J. Chem. Phys.*, 1987, **87**, 6687–6699.
 - 20 D. A. Solis, D. D. Borges, C. F. Woellner and D. S. Galvão, Structural and thermal stability of graphyne and graphdiyne nanoscroll structures, *ACS Appl. Mater. Interfaces*, 2019, **11**, 2670–2676.
 - 21 Q. Li, Y. Chen, F. Du, X. Cui and L. Dai, Bias-free synthesis of hydrogen peroxide from photo-driven oxygen reduction reaction using N-doped γ -graphyne catalyst, *Appl. Catal., B*, 2022, **304**, 120959.
 - 22 B. Wu, H. Jin, J. Yin, W. Zhang, X. Tang, P. Zhang and Y. Ding, Water and salt permeability of monolayer graph-*n*-yne: Molecular dynamics simulations, *Carbon*, 2017, **123**, 688–694.
 - 23 M. Hu, Y. Jing and X. Zhang, Low thermal conductivity of graphyne nanotubes from molecular dynamics study, *Phys. Rev. B: Condens. Matter Mater. Phys.*, 2015, **91**, 155408.
 - 24 A. Ramazani, A. Reihani, A. Soleimani, R. Larson and V. Sundararaghavan, Molecular dynamics study of phonon transport in graphyne nanotubes, *Carbon*, 2017, **123**, 635–644.
 - 25 M. Li, Y. Zhang, Y. Jiang, Y. Zhang, Y. Wang and H. Zhou, Mechanical properties of γ -graphyne nanotubes, *RSC Adv.*, 2018, **8**, 15659–15666.
 - 26 B. Wu, X. Tang, J. Yin, W. Zhang, Y. Jiang, P. Zhang and Y. Ding, Study on mechanical properties of graphyne nanostructures by molecular dynamics simulation, *Mater. Res. Express*, 2017, **4**, 025603.
 - 27 H. Pourmirzaagha, A. Y. Sendi and S. Rouhi, Molecular dynamics simulations of the mechanical properties of two new types of graphyne nanotubes: α -graphyne and α_2 -graphyne nanotubes, *Physica E*, 2020, **119**, 114044.
 - 28 Y. Wang, P. Yuan, M. Li, W. Jiang, Q. Sun and Y. Jia, Calcium-decorated graphyne nanotubes as promising hydrogen storage media: A first-principles study, *J. Solid State Chem.*, 2013, **197**, 323–328.
 - 29 Y. Liu, F. Lu, S. Gao, H. Shi, Y. Mai, L. Zhang, Y. Dai, B. Liao and W. Hu, Density functional theory study on hydrogen storage capacity of yttrium decorated graphyne nanotube, *Int. J. Hydrogen Energy*, 2020, **45**, 10797–10805.
 - 30 Y. Yuan, S. Wu, H. Ai, J. Y. Lee and B. Kang, γ -Graphyne nanotubes as defect-free catalysts of the oxygen reduction reaction: a DFT investigation, *Phys. Chem. Chem. Phys.*, 2020, **22**, 8633–8638.
 - 31 Y. Yuan, J. Ma, H. Ai, B. Kang and J. Y. Lee, A simple general descriptor for rational design of graphyne-based bifunctional electrocatalysts toward hydrogen evolution and oxygen reduction reactions, *J. Colloid Interface Sci.*, 2021, **592**, 440–447.
 - 32 J. Ma, Y. Yuan, S. Wu, J. Y. Lee and B. Kang, γ -Graphyne nanotubes as promising lithium-ion battery anodes, *Appl. Surf. Sci.*, 2020, **531**, 147343.
 - 33 J. Yuan and K. M. Liew, Structural stability of a coaxial carbon nanotube inside a boron–nitride nanotube, *Carbon*, 2011, **49**, 677–683.
 - 34 R. Xiang, T. Inoue, Y. Zheng, A. Kumamoto, Y. Qian, Y. Sato, M. Liu, D. Tang, D. Gokhale, J. Guo, K. Hisama, S. Yotsumoto, T. Ogimoto, H. Arai, Y. Kobayashi, H. Zhang, B. Hou, A. Anisimov, M. Maruyama, Y. Miyata, S. Okada, S. Chiashi, Y. Li, J. Kong, E. I. Kauppinen, Y. Ikuhara, K. Suenaga and S. Maruyama, One-dimensional van der Waals heterostructures, *Science*, 2020, **367**, 537–542.
 - 35 H. Ghaderi, A. Ghasemi, S. Rouhi and E. Mahdavi, Evaluation of the thermal conductivity coefficient of the strained concentric multi-walled carbon and boron-nitride nanotubes: A molecular dynamics investigation, *Physica E*, 2021, **134**, 114830.
 - 36 P. Ying, J. Zhang, Y. Du and Z. Zhong, Effects of coating layers on the thermal transport in carbon nanotubes-based van der Waals heterostructures, *Carbon*, 2021, **176**, 446–457.
 - 37 Y. Lv, X. Wu, H. Lin, J. Li, H. Zhang, J. Guo, D. Jia and H. Zhang, A novel carbon support: Few-layered graphdiyne-decorated carbon nanotubes capture metal clusters as effective metal-supported catalysts, *Small*, 2021, **17**, 2006442.
 - 38 C. Li and T. Chou, Elastic moduli of multi-walled carbon nanotubes and the effect of van der Waals force, *Compos. Sci. Technol.*, 2003, **63**, 1517–1524.
 - 39 S. Ajori, S. H. Boroushak, R. Hassani and R. Ansari, A molecular dynamics study on the buckling behavior of x-graphyne based single- and multi-walled nanotubes, *Comp., Mater. Sci.*, 2021, **191**, 110333.
 - 40 A. P. Thompson, H. M. Aktulgä, R. Berger, D. S. Bolintineanu, W. M. Brown, P. S. Crozier, P. J. In't Veld, A. Kohlmeyer, S. G. Moore, T. D. Nguyen, R. Shan, M. J. Stevens, J. Tranchida, C. Trott and S. J. Plimpton, LAMMPS - a flexible simulation tool for particle-based materials modeling at the atomic, meso, and continuum scales, *Comput. Phys. Commun.*, 2022, **271**, 108171.
 - 41 D. W. Brenner, O. A. Shenderova, J. A. Harrison, S. J. Stuart, B. Ni and S. B. Sinnott, A second-generation reactive empirical bond order (REBO) potential energy expression for hydrocarbons, *J. Phys.: Condens. Matter*, 2002, **14**, 783–802.
 - 42 B. Azizi, S. Rezaee, M. J. Hadianfar and K. H. Dehnou, A comprehensive study on the mechanical properties and failure mechanisms of graphyne nanotubes (GNTs) in different phases, *Comput. Mater. Sci.*, 2020, **182**, 109794.
 - 43 K. Min and N. R. Aluru, Mechanical properties of graphene under shear deformation, *Appl. Phys. Lett.*, 2011, **98**, 013113.
 - 44 A. R. Alian and S. A. Meguid, A critical study of the parameters governing molecular dynamics simulations of nanostructured materials, *Comp., Mater. Sci.*, 2018, **153**, 183–199.
 - 45 W. G. Hoover, Canonical dynamics: Equilibrium phase-space distributions, *Phys. Rev. A: At., Mol., Opt. Phys.*, 1985, **31**, 1695–1697.
 - 46 H. Zhao, D. Wei, L. Zhou, H. Shi and X. Zhou, Thermal conductivities of graphyne nanotubes from atomistic simulations, *Comput. Mater. Sci.*, 2015, **106**, 69–75.
 - 47 G. Lei, H. Cheng, H. Liu and W. Rao, Thermal rectification in asymmetric graphyne nanoribbons: A nonequilibrium molecular dynamics study, *Mater. Lett.*, 2017, **189**, 101–103.

- 48 T. Schneider and E. Stoll, Molecular-dynamics study of a three-dimensional one-component model for distortive phase transitions, *Phys. Rev. B: Condens. Matter Mater. Phys.*, 1978, **17**, 1302–1322.
- 49 T. Ikeshoji and B. R. Hafskjold, Non-equilibrium molecular dynamics calculation of heat conduction in liquid and through liquid-gas interface, *Mol. Phys.*, 1994, **81**, 251–261.
- 50 Y. Huang, J. Wu and K. C. Hwang, Thickness of graphene and single-wall carbon nanotubes, *Phys. Rev. B: Condens. Matter Mater. Phys.*, 2006, **74**, 245413.
- 51 C. Li and T. Chou, Elastic moduli of multi-walled carbon nanotubes and the effect of van der Waals forces, *Compos. Sci. Technol.*, 2003, **63**, 1517–1524.
- 52 J. Shiomi and S. Maruyama, Molecular dynamics of diffusive-ballistic heat conduction in single-walled carbon nanotubes, *Jpn. J. Appl. Phys.*, 2008, **47**, 2005–2009.
- 53 D. Yang, Q. Zhang, G. Chen, S. F. Yoon, J. Ahn, S. Wang, Q. Zhou, Q. Wang and J. Li, Thermal conductivity of multi-walled carbon nanotubes, *Phys. Rev. B: Condens. Matter Mater. Phys.*, 2002, **66**, 165440.
- 54 P. K. Schelling, S. R. Phillipot and P. Keblinski, Comparison of atomic-level simulation methods for computing thermal conductivity, *Phys. Rev. B: Condens. Matter Mater. Phys.*, 2002, **65**, 144306.
- 55 H. Xie, T. Ouyang, É. Germaneau, G. Qin, M. Hu and H. Bao, Large tunability of lattice thermal conductivity of monolayer silicene *via* mechanical strain, *Phys. Rev. B: Condens. Matter Mater. Phys.*, 2016, **93**, 075404.
- 56 M. Ohnishi and J. Shiomi, Strain-induced band modulation of thermal phonons in carbon nanotubes, *Phys. Rev. B*, 2021, **104**, 014306.
- 57 J. M. Dickey and A. Paskin, Computer Simulation of the Lattice Dynamics of Solids, *Phys. Rev.*, 1969, **188**, 1407–1418.
- 58 C. Kittel and R. W. Hellwarth, *Introduction to solid state physics*, Wiley, New York, 8th edn, 2005.
- 59 Z. Xu and M. J. Buehler, Strain controlled thermomutability of single-walled carbon nanotubes, *Nanotechnology*, 2009, **20**, 185701.
- 60 X. Li, K. Maute, M. L. Dunn and R. Yang, Strain effects on the thermal conductivity of nanostructures, *Phys. Rev. B: Condens. Matter Mater. Phys.*, 2010, **81**, 245318.
- 61 J. A. Thomas, J. E. Turney, R. M. Iutzi, C. H. Amon and A. J. H. McGaughey, Predicting phonon dispersion relations and lifetimes from the spectral energy density, *Phys. Rev. B: Condens. Matter Mater. Phys.*, 2010, **81**, 081411.